JGR

RESEARCH ARTICLE

Key Points:
- Localized orographic sources create mountain waves which can propagate as high as the mesosphere
- These waves carry large amount of momentum
- They eventually break and release this momentum in the atmosphere

Correspondence to:
P.-D. Pautet,
dominiquepautet@gmail.com

Large-amplitude mesospheric response to an orographic wave generated over the Southern Ocean Auckland Islands (50.7°S) during the DEEPWAVE project

P.-D. Pautet[1], M. J. Taylor[1], D. C. Fritts[2], K. Bossert[2], B. P. Williams[2], D. Broutman[3], J. Ma[3], S. D. Eckermann[4], and J. D. Doyle[5]

[1]Center for Atmospheric and Space Science, Utah State University, Logan, Utah, USA, [2]GATS, Inc., Boulder, Colorado, USA, [3]Computational Physics, Inc., Springfield, Virginia, USA, [4]E.O. Hulburt Center for Space Research, Naval Research Laboratory, Washington, District of Columbia, USA, [5]Naval Research Laboratory, Monterey, California, USA

Abstract The Deep Propagating Gravity Wave Experiment (DEEPWAVE) project was conducted over New Zealand and the surrounding regions during June and July 2014, to more fully understand the generation, propagation, and effects of atmospheric gravity waves. A large suite of instruments collected data from the ground to the upper atmosphere (~100 km), with several new remote-sensing instruments operating on board the NSF Gulfstream V (GV) research aircraft, which was the central measurement platform of the project. On 14 July, during one of the research flights (research flight 23), a spectacular event was observed as the GV flew in the lee of the sub-Antarctic Auckland Islands (50.7°S). An apparent "ship wave" pattern was imaged in the OH layer (at ~83.5 km) by the Utah State University Advanced Mesospheric Temperature Mapper and evolved significantly over four successive passes spanning more than 4 h. The waves were associated with orographic forcing generated by relatively strong (15–20 m/s) near-surface wind flowing over the rugged island topography. The mountain wave had an amplitude $T' \sim 10$ K, a dominant horizontal wavelength ~40 km, achieved a momentum flux exceeding $300 \, \text{m}^2 \, \text{s}^{-2}$, and eventually exhibited instability and breaking at the OH altitude. This case of deep mountain wave propagation demonstrates the potential for strong responses in the mesosphere arising from a small source under suitable propagation conditions and suggests that such cases may be more common than previously believed.

1. Introduction

Gravity waves (GWs) are well recognized as one of the main drivers of Earth's atmosphere and have influences that typically increase into the mesosphere/lower thermosphere (MLT). Their major influences in the MLT result from their large increases in amplitude over many scale heights and their efficient transport of energy and momentum from source altitudes to the altitudes at which they dissipate. These dynamics are believed to have large effects on the mean structures, tides, and planetary waves throughout the MLT and at higher altitudes [*Fritts and Alexander*, 2003; *Yiğit and Medvedev*, 2010]. However, these effects are poorly described in global models at present due to our very qualitative understanding of the GW dynamics and statistics having the major influences in the MLT and above [e.g., *Kim et al.*, 2003].

Most GWs observed in the MLT originate at lower altitudes where they are generated by a wide variety of sources [e.g., *Fritts and Alexander*, 2003]. Deep convection appears as a major GW source, based on observations extending into the stratosphere [*Fritts and Nastrom*, 1992; *Wu and Waters*, 1996; *Dewan et al.*, 1998; *Tsuda et al.*, 2000] and in the MLT [e.g., *Taylor and Hapgood*, 1988; *Hocke and Tsuda*, 2001; *Sentman et al.*, 2003; *Vadas et al.*, 2009; *Yue et al.*, 2009]. Another major source of GWs that penetrate into the stratosphere and higher, especially in specific regions during winter, is significant orography at large and small spatial scales [*Fritts and Nastrom*, 1992; *Sato*, 1994; *Eckermann and Preusse*, 1999; *Wu et al.*, 2006; *Plougonven et al.*, 2008; *Alexander et al.*, 2009; *Smith et al.*, 2009; *Alexander and Grimsdell*, 2013; *Hendricks et al.*, 2014; *Vosper*, 2015]. Other sources for which there is significant evidence include frontal systems [*Reeder and Griffiths*, 1996], jet streams [*Luo and Fritts*, 1993; *Guest et al.*, 2000; *Plougonven et al.*, 2003], wave-wave interactions [*Bretherton*, 1969; *Yeh and Liu*, 1981; *Dunkerton*, 1987], and secondary generation accompanying GW breaking and strong local body forcing [*Vadas and Fritts*, 2002]. Importantly, a number of studies have revealed intermittent GWs having large amplitudes and momentum fluxes in the stratosphere and MLT [*Fritts et al.*, 2002,

2014; *Hertzog et al.*, 2012; *Jewtoukoff et al.*, 2013; *Bossert et al.*, 2015] that appear to contribute a large fraction of the total momentum flux at each altitude.

The Deep Propagating Gravity Wave Experiment (DEEPWAVE) was performed specifically to address these various topics through comprehensive, multi-instrument observations and associated modeling extending from the ground to ~100 km (see *Fritts et al.* [2015] for an overview) in a region containing all of the major GW sources in the lower atmosphere. The initial results include a number of interesting responses of high relevance to the current study and to MLT GW influences more generally. Specifically, they reveal that MLT mountain waves (MWs) (1) can achieve large amplitudes, implying large momentum fluxes, at large and small horizontal wavelengths in response to weak surface forcing, (2) often exceed the amplitudes due to other GW sources, and (3) have responses that often extend over a much larger area than the underlying terrain [*Fritts et al.*, 2015; *Bossert et al.*, 2015].

This paper presents a surprising example of mesospheric MW observations associated with orographic forcing over the small sub-Antarctic Auckland Islands archipelago. We provide a short overview of the DEEPWAVE project during which the measurements were made and describe the instrumentation operated on board the Gulfstream V (GV) in section 2. Observations made during research flight #23 (RF23) are presented and discussed in section 3. A discussion of the results and our conclusions are presented in sections 4 and 5, respectively.

2. DEEPWAVE Overview and New GV Airborne Instrumentation

2.1. DEEPWAVE Overview

The Deep Propagating Gravity Wave Experiment (DEEPWAVE) was designed to better understand GW generation, propagation, and effects from their sources to their regions of dissipation, which are typically in the stratosphere or MLT, depending on the GW amplitudes at lower altitudes and the environments through which they propagate. The airborne component of the DEEPWAVE campaign was based in Christchurch, New Zealand. It took place from 6 June to 21 July 2014, period during which the middle atmosphere background conditions during the winter months (eastward wind) allow deep GW propagation.

Several ground-based sites on South Island and elsewhere hosted multiple instruments (radiosondes, Rayleigh lidar, airglow imagers, Fabry-Perot spectrometer, and radar), but the centerpiece of the project was the GV. Its long-range capability (~9000 km), cruising altitude (~12 km), and instrument suite allowed it to sample many regions of interest, depending on the forecasted GW sources (orography, convection, frontal system, and jet stream) and propagation environment. Onboard instruments measured atmospheric parameters below the aircraft (dropsondes), at flight altitude (temperature, pressure, and horizontal and vertical winds), and also remotely in the stratosphere (Rayleigh lidar), and in the MLT region (Na lidar, Advanced Mesospheric Temperature Mapper, and IR OH airglow imagers). The mesospheric instruments are described in more detail below. In addition, the Atmospheric Infrared Sounder instrument on board the AQUA satellite [*Aumann et al.*, 2003] provided near real-time temperature-sensitive radiances from ~20 to 42 km in the stratosphere, from which gravity wave maps were derived. Finally, several high-resolution forecast models provided daily guidance in flight planning throughout the flight program. A more complete description of the DEEPWAVE project and several initial research highlights are given by *Fritts et al.* [2015].

2.2. New GV Airborne Instrumentation

Several new remote-sensing instruments were built specifically to expand the GV measurement capabilities to ~100 km for DEEPWAVE. An Advanced Mesospheric Temperature Mapper (AMTM) measured the atmospheric temperature over a ~120 × 80 km region centered near zenith, using the OH (3,1) band emission. This bright emission originates from a ~7–8 km thick layer located at ~87 km and is widely used as a tracer of the dynamical processes in the MLT. The AMTM was designed and built at Utah State University (USU). It uses a 320 × 256 pixel infrared (IR) sensor and a computer-controlled filter wheel to sequentially measure the brightness of the $P_1(2)$ and $P_1(4)$ lines of the OH (3,1) band, as well as the atmospheric background. Combining these three emissions, it is possible to process the OH (3,1) rotational temperature for each pixel of an image and "map" the mesospheric temperature over a large region. More details about this instrument are given in *Pautet et al.* [2014]. In addition to the AMTM, two low-elevation (field of view centered at 25° elevation angle) IR imagers were installed on each side of the plane. They measured only the OH emission
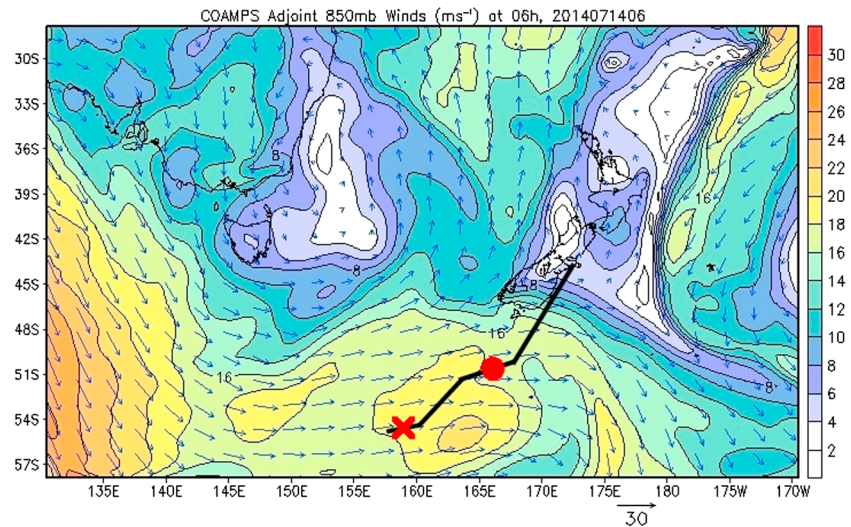
Figure 1. The Naval Research Laboratory (NRL) Coupled Ocean-Atmosphere Mesoscale Prediction System (COAMPS) forecast showing the tropospheric wind at 850 hPa at 0600 UTC on 14 July for the DEEPWAVE region of interest. Auckland Islands are indicated by the red dot, while Macquarie Island corresponds to the red cross. The flight path for RF23 is shown as a black line.

brightness, but their wide field of view (~40 × 30°) provided the larger-scale context for the vertically viewing lidar and AMTM measurements in the MLT.

A new Rayleigh lidar provided vertical profiles of density from which temperatures were inferred from ~20 to 60 km. A new Na lidar provided measurements of Na densities and temperatures from ~72 to ~105 km, depending on the degree of variability in the Na layer. These two lidars were built as new GV facility instruments by GATS and were contained in two standard GV instrument racks.

The Rayleigh lidar data processing followed the normal Rayleigh procedure, and then an atmospheric density profile is calculated from the lidar signal profile taking into account the geometric factors. The density is integrated down from a temperature at 71 km provided by operational analysis of the European Centre for Medium-Range Weather Forecasts Integrated Forecast System and interpolated to the aircraft time and location. This procedure yields temperature profiles extending down to ~20 km, below which aerosol backscatter causes biases. For reference, the temperature error is ~2 K for a 30 s integration over 3 km vertical layers at ~40 km. More information about this instrument is given in *Bossert et al.* [2015].

The GV sodium lidar is a high spectral resolution system that shared the same racks, telescope, and receiver electronics as the Rayleigh lidar. The transmitter is a narrowband Toptica continuous-wave laser composed of an 18 W Raman fiber amplifier doubled to produce 10 W of 589 nm light with a 10 MHz line width. The laser output light is locked to the D2a feature in the sodium Doppler-free saturation spectrum. An acousto-optic amplitude modulator produces 20 μs square pulses repeating at 1 kHz. This pulsed beam has a 150 km total range and 3 km range resolution. It is synchronized with the Rayleigh beam to avoid cross talk, and the data are recorded on the same counter board oversampled at 1 s and 37.5 m sampling. For postprocessing, the counts are averaged in bins of 900 m vertically and 48 s (~11.5 km spatially, depending on aircraft speed) and Rayleigh normalized at altitudes from 30 to 35 km using Mass Spectrometer Incoherent Scatter (MSIS) (The signal in the Na layer is divided by the signal near 30 km to take out lower atmosphere transmission variations and multiplied by the ratio of scattering cross sections, corrected for $1/r^2$ assuming a density near 30 km from MSIS to get the Na density.). The mixing ratios are calculated from sodium densities and relative background atmospheric conditions based on a scale height calculated from the AMTM temperature and MSIS densities at 87 km.

2.3. Flight Altitude Measurements

In addition to the instruments described above, the GV aircraft is equipped to record all the relevant flight information (coordinates, altitude, speed, heading, roll, pitch, etc.) and to measure the parameters
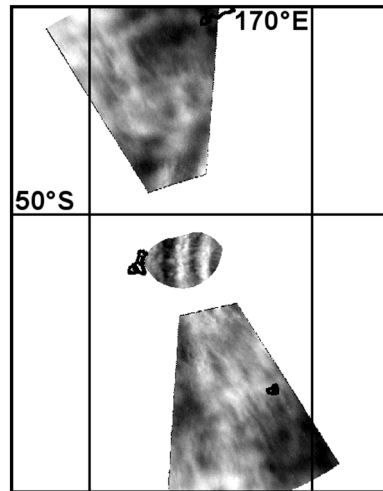
Figure 2. OH brightness measured simultaneously by the three imagers operating on board the GV aircraft at 0656 UTC during RF23. Large amplitude waves are visible east of AI.

characterizing the surrounding atmosphere (pressure, temperature, and horizontal and vertical winds) at 1 Hz (low rate) frequency, with the capability to provide 25 Hz data. These measurements provide additional information on GWs and their environment at flight altitude.

3. Observations

A total of 26 GV research flights were conducted during the DEEPWAVE campaign. The significant range of the GV aircraft (~9000 km) allowed measurements over large regions in the vicinity of New Zealand, targeting specific GW sources or propagation conditions. On 14 July, the orographic forcing over the South Island was relatively weak but a region of moderate tropospheric wind (~20–25 m/s at 850 hPa) was forecast over the Southern Ocean, as shown in Figure 1. A small isolated uninhabited archipelago named Auckland Islands (AI) is located in this area (50.7°S, 166.1°E, red dot on the map). Its size (~30 × 80 km) and terrain elevation (up to 660 m) made it a good candidate for the generation of mountain waves which could potentially
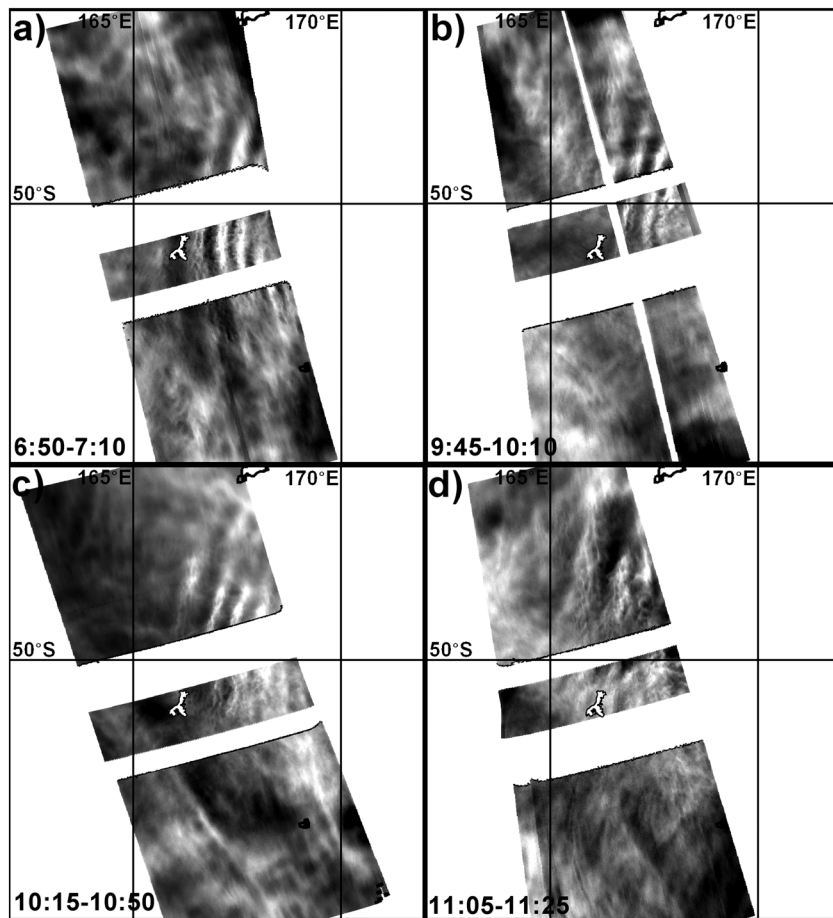

Figure 3. OH brightness mapping corresponding to the four legs flown over the AI and showing the evolution and decay of the orographic waves generated by flow over the Auckland Islands terrain (a) between 0650 and 0710 UTC, (b) between 0945 and 1010 UTC, (c) between 1015 and 1050 UTC, and (d) between 1105 and 1125 UTC.
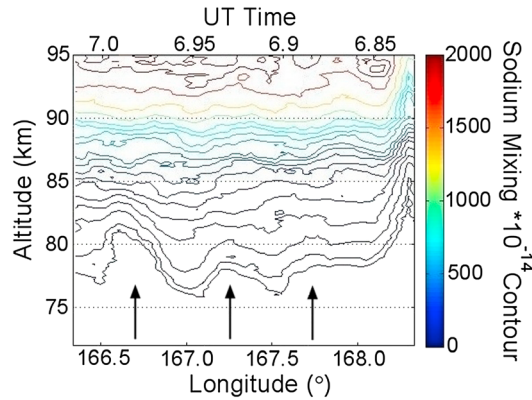
Figure 4. Na mixing ratio contour measured by the Na lidar as the GV flew over AI between 0650 and 0700 UTC. The vertical, slightly tilted structures (indicated by the vertical arrows) correspond to the waves observed simultaneously by the AMTM.

propagate deep into the atmosphere, based on DEEPWAVE forecasts. Another small island in the Southern Ocean, named Macquarie Island, is located farther south (54.6°S, 158.9°E, red cross on the map), but its lower altitude and narrower topography were considered less likely to create mountain waves with a sufficiently large amplitude to be observed at high altitudes. Nevertheless, it was decided to fly over both potential sources to observe the possible MW responses created by the near-surface wind over those two islands. Four passes over each island were performed on this research flight 23 (RF23), and its flight path is shown as a black line in Figure 1.

RF23 lasted from 0545 UTC to 1230 UTC on 14 July 2014. At 0645 UTC, as the aircraft was approaching the AI from the north-east, real-time AMTM images exhibited large-amplitude waves in the OH layer on the lee side of the archipelago. Figure 2 shows the OH brightness measured simultaneously by the AMTM and two IR cameras at 0656 UTC and projected on a geographical map. Several crests are visible in the zenith imager field of view. They also extend farther north, into the region observed by the right wing camera. In contrast, no sign of this feature appears south of the flight track. As the GV passed over AI and kept moving west, the apparent MW disappeared. Two and half hours later, the aircraft came back and flew a second time over AI. The same MW patterns were still present, but they had begun to exhibit evidence of breaking in the zenith field of view. The very small scale structures visible within the large-amplitude MW are typical of a wave breaking event, with accompanying irreversible momentum deposition in the atmosphere [e.g., *Yamada et al.*, 2001; *Fritts et al.*, 2002]. The GV flew two more legs over the archipelago in order to follow the evolution and decay of this MW event. Figure 3 shows the OH brightness mapping corresponding to the four passes over AI. Between 0650 and 0710 UTC (Figure 3a), a "ship wave" pattern is imaged to the east (lee side) of the AI. No other GWs are visible in this region. Two and half hours later (Figure 3b), the waves are still at the same location but also extend slightly farther to the north. They also exhibit evidence of breaking in the AMTM field of view. During the third leg (Figure 3c), the MW in the zenith field of view has largely disappeared. However, it is still visible with a large amplitude farther north, in the field of view of the right wing camera. Finally, when the aircraft flew for the last time over the islands between 1105 and 1125 UTC
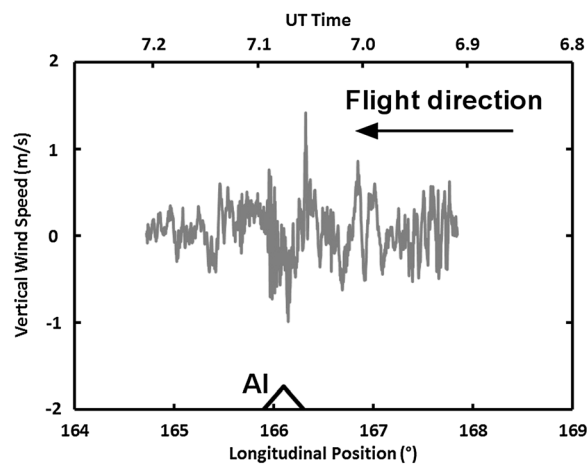
(Figure 3d), images revealed an apparently dissipating MW exhibiting significant instability features to the north. Over the duration of the flight (~6 h), this large-amplitude MW remained in the same location, and was nearly stationary, until it broke, yielding instabilities and turbulence, and disappeared.

This MW event was also visible in the vertical profiles obtained by the GV Na lidar. Figure 4 shows the Na mixing ratio contours measured at zenith along the GV flight path during the first leg over the AI. The large-tilted features (arrows) correspond to the locations and wavelengths of the MW temperature perturbations observed with the AMTM. Unfortunately, the lidars had to be turned off for the following overpasses due to aircraft regulations, as the GV was flying at a lower altitude in order to make in situ measurements closer to the MW source.
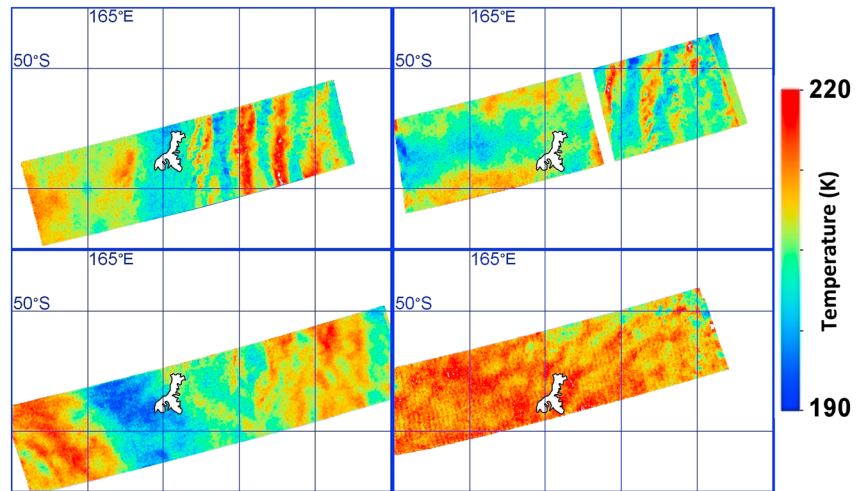

Figure 5. Vertical wind velocity measured at flight altitude (11.9 km) during the first leg over AI. The position of the island is indicated at the bottom.

Figure 6. AMTM temperature mapping showing the absolute temperature perturbations at the MLT altitude over the Gulfstream V flight path. Times are the same as in Figure 3.

In addition to the middle and upper atmosphere data, several instruments on board the aircraft recorded in situ atmospheric parameters while flying over the AI terrain. Figure 5 shows the vertical wind velocity measured at the aircraft altitude (~11.9 km) during the first leg. Oscillations with amplitude of ~1 m/s are visible over and on the lee side of the AI topography, represented at the bottom of the plot. Subsequent passes (not shown) exhibited similar perturbations but with decreasing amplitude as the wind was weakening over the island terrain.

3.1. Temperature Maps

The AMTM is not only able to measure the OH brightness, but it can also be used to determine the OH rotational temperature (as noted in section 2.1), thus providing a temperature map at the OH altitude every ~16 s. Figure 6 shows a series of four temperature mappings corresponding to each leg over AI. The parameters of the temperature oscillations can easily be measured. In the case of leg #1, the horizontal wavelength λ_x was 40 ± 3 km, the apparent temperature perturbation $<T'>$ (where angle brackets denote averaging over the OH layer), exhibited a 10 ± 1 K amplitude for an average temperature T_0 of 205 ± 1 K, and the direction orthogonal to the MW phase structure θ was equal to $90 \pm 5°$ anticlockwise from due north. As already seen in Figure 3, the MW perturbations remained approximately at the same location and had a horizontal phase speed c near zero throughout the RF23 flight segments over the AI.

4. Discussion

As GWs propagate upward, they transport momentum that resides in the background atmosphere via a pseudomomentum flux (MF) [*Fritts and Alexander*, 2003]. The MF per unit mass for a given wave can be calculated knowing its parameters, as well as the background conditions, using the following equation [*Fritts et al.*, 2014]:

$$<u_h'w'> = \frac{g^2 \omega_i}{2N^3} \sqrt{1 - \frac{\omega_i^2}{N^2}} \left(\frac{<T'>}{T_0} \right)^2 \frac{1}{C^2} \tag{1}$$

Here g is the acceleration of gravity (9.54 m s^{-2} at the OH layer), N is the buoyancy frequency, ω_i is the intrinsic frequency of the GW, $<T'>$ is the measured temperature perturbation amplitude, T_0 the mean temperature at the altitude of the OH (3,1) emission, and C is a factor to compensate for the phase averaging over the finite thickness of the OH layer. It is defined by

$$C = \frac{<T'>}{T'(z_0)} = \exp\left(-3.56 \frac{z_{FWHM}^2}{\lambda_z^2} \right) \tag{2}$$

where z_{FWHM} is the full width at half maximum OH layer thickness and λ_z is the vertical GW wavelength. The triangular parentheses in (1) represent means over both the airglow layer and a complete wave oscillation.
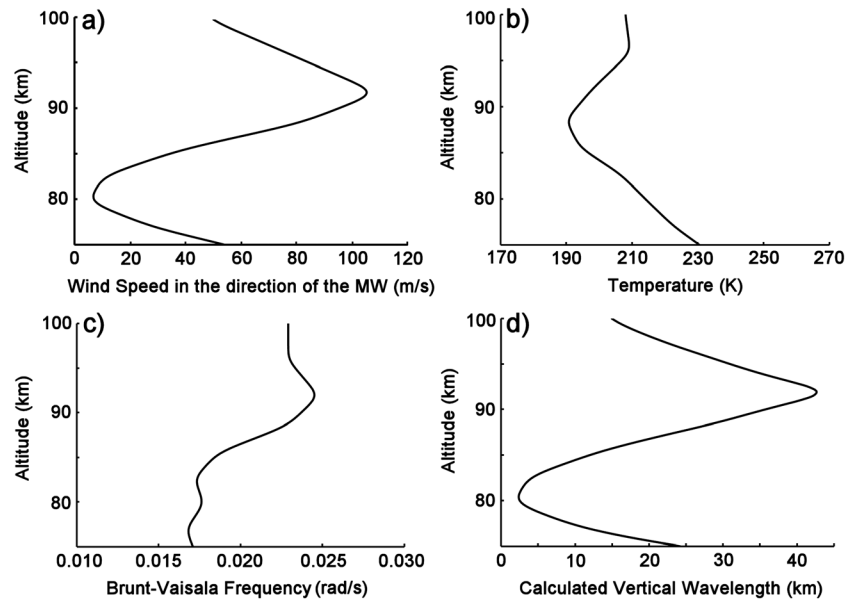
Figure 7. NAVGEM reanalysis data between 75 and 100 km over the AI area at 0900 UTC, for the wind in (a) the MW direction, (b) the temperature, and (c) the Brunt-Väisälä frequency. (d) The calculated vertical wavelength for the MW observed over the AI.

During the DEEPWAVE flights, the AMTM instrument provided direct measurements of the GW horizontal parameters (wavelength λ_h, observed phase speed c, temperature perturbation $<T'>$, and GW azimuthal orientation θ). The vertical temperature profiles in the MLT region were given, when possible, by the GV Na lidar, while the Navy Global Environmental Model (NAVGEM) reanalysis model supplied the background wind data over the oceanic regions, where no instruments (e.g., radar, spectrometer, or wind lidar) were available.

The Navy Global Environmental Model (NAVGEM) is the navy's operational global numerical weather prediction system [*Hogan et al.*, 2014; *Eckermann et al.*, 2014]. For DEEPWAVE, the complete NAVGEM system was rerun in a reanalysis configuration for the entire austral winter of 2014 using a high-altitude research configuration extending to ~100 km altitude. In addition to the full suite of operational sensor data, the reanalysis assimilated high-altitude satellite data from the SABER (Sounding of the Atmosphere Using Broadband Emission Radiometry), Microwave Limb Sounder, and Special Sensor Microwave Imager/Sounder instruments, leveraging earlier high-altitude data assimilation work described in *Eckermann et al.* [2009] and *Hoppel et al.* [2013]. The reanalysis profiles also include wind data from the three GV dropsondes released over Auckland Island during RF23. Further details are provided in (D. Broutman et al., Fourier modeling of mesospheric mountain waves observed near Auckland Island during the Deep Propagating Gravity Wave Experiment (DEEPWAVE), *Journal Atmospheric Science*, under review, 2016).

Figure 7 shows the NAVGEM horizontal wind in the direction of the wave (a), the temperature (b), and the Brunt-Väisälä frequency (c) vertical profiles between 75 and 100 km, at 12 UT on 14 July, averaged over a ~140 × 110 km region surrounding the AI. In order to solve equation (1), the background parameters deduced from the vertical profiles have to be integrated, weighted by brightness, over the OH layer, but its altitude may vary depending on seasonal and dynamical conditions. The SABER instrument on board the thermosphere-ionosphere-mesosphere electrodynamics (TIMED) satellite measures OH density profiles that help define the altitude of the OH layer. Such a profile (not shown) was obtained at 1250 UTC on 14 July 2014, at coordinates 50.7°S, 171.2°E (~360 km east of AI). According to this measurement, the center of the OH layer that night, in this area, was at 84.0 ± 0.5 km, and the full width at half maximum (FWHM) was ~7.5 km. In fact, this profile corresponds to a channel at 1.6 µm (comprising the OH (4,2) and (5,3) bands). If the difference in altitude between the OH emission bands is taken into account [*von Savigny et al.*, 2012], the perturbations observed by the AMTM originated from a layer centered at 83.5 ± 0.5 km with FWHM ~7.5 km.

The NAVGEM horizontal wind profile in the direction of the wave (Figure 7a) shows a minimum (~7 m/s) at ~80.5 km. As the wind decreases in speed with height, the wave refracts to smaller vertical wavelengths with

a smaller intrinsic phase speed, which is equal to the horizontal wind speed in the case of stationary MWs. To confirm this possibility, the vertical wave number of the GW was calculated using the following equation [*Nappo*, 2002]:

$$m^2 = \frac{N^2}{c_i^2} + \frac{u''_0}{c_i} - \frac{1}{H_S}\frac{u'_0}{c_i} - \frac{1}{4H_S^2} - k^2 \qquad (3)$$

where N is the buoyancy frequency, c_i is the intrinsic phase speed, u'_0 and u''_0 are the first and second vertical derivatives of the horizontal wind speed in the direction of the wave, H_s is the scale height ($=R \cdot T/g$, with $R = 287\,\mathrm{J\,kg^{-1}\,K^{-1}}$), and k is the wave horizontal wave number.

The vertical wavelength is then equal to

$$\lambda_z = \frac{2\pi}{m} \qquad (4)$$

Figure 7d shows the vertical profile for λ_z, calculated using the NAVGEM background information and the AMTM horizontal wave parameters. As expected, the GW came close to a critical level just above 80 km, with its vertical wavelength decreasing to less than 5 km. Another way to estimate λ_z is to use the Na density plot (Figure 4). This contour plot was made using lidar data averaged over 48 s (or ~11.5 km horizontally) and 900 m vertically. The tilt of the wave clearly changed when approaching the 80 km level, implying a decrease of the vertical wavelength. For example, the first crest is only slightly tilted toward the left below 78 km. At that point, the corresponding vertical wavelength [*Vadas and Nicolls*, 2009] is still larger than 20 km. Above that altitude, the inclination of the wave decreases, indicating a diminution of λ_z to ~12 km.

The vertical wavelength has a large impact on the MF calculation, especially when it approaches the FWHM of the OH layer (~7.5 km), as it strongly affects the phase averaging through the factor C (equation (2)). Nevertheless, it is still possible to give an estimate of the MF associated with this MW using equation (1), but employing the MW vertical displacement directly, rather than an indirect T' estimate derived from $<T'>$ and guessing at λ_z and C.

Using equation (1) with $C \sim 1$ and T' inferred from an apparent maximum vertical displacement of ~2.5 km at ~78 km altitude, e.g., $\delta_z > 2.5$ km, an implied $\lambda_z > 16$ km and $T' > 16$ K, $N \sim 0.017\,\mathrm{s^{-1}}$ from NAVGEM (Figure 7c), and a minimum $\omega_i \sim 0.37\,N$, we obtain an estimate of the minimum MF of ~320 $\mathrm{m^2\,s^{-2}}$ for this event.

In fact, the goal of this estimation is more on demonstrating the large impact of this wave on the MLT region than determining precisely the value of the MF transported by this single GW. This conservative estimate is extremely large relative to previous mesospheric studies investigating the mean MF carried by GWs in the MLT. For example, mesospheric radar data obtained during an 8 day period from Adelaide, Australia [*Fritts and Vincent*, 1987], yielded values $<5\,\mathrm{m^2\,s^{-2}}$. More recently, *Placke et al.* [2015] compared 4 years of measurements from two different radar systems (MF and meteor), located in Northern Norway. They used two different analysis techniques and found similar values and variabilities for the mesospheric MF, with average numbers $<10\,\mathrm{m^2\,s^{-2}}$. Another method to approximate MF employing airglow brightness image data [*Gardner et al.*, 1999] has been used in several studies, and most of them inferred small mean MF values. This method defines a simple relation between the airglow emission brightness fluctuations and the temperature perturbations. *Hickey and Yu* [2005] have shown that airglow brightness and temperature perturbations are not so easily related to each other. The cancelation factor used by *Gardner et al.* [1999] may vary by a factor of 2–10 between models, depending on the GW phase speeds, implying a factor of 4–100 in the estimation of the GW fluxes. Nevertheless, comparison with studies employing this method gives a general idea about the average MF carried by small-scale GWs at the MLT altitude. For example, *Swenson et al.* [1999], who compared imager and Na lidar data over a 5 day period, measured mean MFs of 1.9 $\mathrm{m^2\,s^{-2}}$ with the imager and 13.3 $\mathrm{m^2\,s^{-2}}$ with the lidar (but for longer GW periods). *Tang et al.* [2002] measured average wintertime fluxes of 20 $\mathrm{m^2\,s^{-2}}$ and 12 $\mathrm{m^2\,s^{-2}}$, at 35°N, in the zonal and meridional directions, respectively. Using image data acquired in Antarctica, *Espy et al.* [2006] obtained mean fluxes of 7.5 $\mathrm{m^2\,s^{-2}}$ and 1.6 $\mathrm{m^2\,s^{-2}}$ in the zonal and meridional directions, respectively, over Halley station (75.5°S) but somewhat larger values (32 and 4 $\mathrm{m^2\,s^{-2}}$) over Rothera station (67.5°S). Their results show important site-to-site and day-to-day variabilities which they attributed to regional differences due to stronger sources and seasonal wind filtering. Finally, *Li et al.* [2011], who analyzed image data obtained during 5 years on the Maui Island (20.8°N), found average monthly values
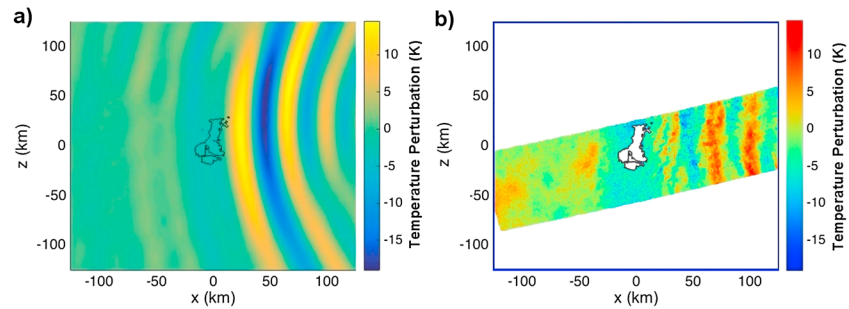
Figure 8. (a) Wave-induced temperature perturbations at 77 km altitude from a Fourier simulation after 2 h using NAVGEM reanalysis fields at 0600 UTC upstream of Auckland Island (D. Broutman et al., under review, 2016) and (b) AMTM zenith temperature measurements with similar spatial and temperature scales as in Figure 8a.

on the order of $10\,m^2\,s^{-2}$. Most of the GWs propagating through the MLT region carry relatively small MF, but some specific, localized events may carry much larger values. Previous mesospheric measurements of isolated GW events yielded MF of the same order of magnitude as the one over AI. In an estimation of the spectacular gravity wave breaking event described by *Yamada et al.* [2001], *Fritts et al.* [2002] calculated its MF to be ~$900\,m^2\,s^{-2}$. Similarly, *Fritts et al.* [2014] measured a MF close to $800\,m^2\,s^{-2}$ for a GW packet observed by another AMTM instrument over the Arctic Lidar Observatory for Middle Atmosphere Research (ALOMAR) facility, Norway. These events, as well as recent stratospheric balloon measurements [*Hertzog et al.*, 2012], suggest that there are sporadic, but not infrequent, very strong flux events, typically at the smaller horizontal scales and higher frequencies, which should be expected at the MLT altitudes. The AI MW event documented here provides further evidence of those.

The GW event detected over the Auckland Islands lasted at least 4 h and exhibited features suggesting that wave breaking was occurring at the altitude of the OH layer. Figure 6 illustrates the progression of the short-scale structures: first, they were only visible on the crest closest to the island (a), then they covered the whole wave packet (b), and finally, they vanished, as well as the GW itself (c–d). At that point, the wave had disappeared, releasing its large momentum into the atmospheric background. The GW's impact on the atmosphere is still not fully understood, especially the momentum deposition, but the effect of a moderate tropospheric wind (~25 m/s, while *Smith et al.* [2009] reported wind up to 70 m/s over the Andes to generate the waves they observed in the mesosphere) generating orographic forcing on a small isolated mountain appears to yield significant MLT impacts. Although recent progress has been made, actual models are still limited in their resolution and cannot globally represent the effect of small-scale GWs. Small topographies like AI are not resolved either, even if they appear to be a possible recurrent source of momentum able to propagate deep into the atmosphere, especially during the winter months. The example presented in this paper clearly shows that such small sources have to be investigated more deeply to better understand their effect and to improve parametrizations of subgrid-scale orographic gravity wave drag used in models.

In a companion paper, D. Broutman et al. (under review, 2016) apply a Fourier method to model mountain waves generated by Auckland Island during the DEEPWAVE experiment using reanalysis profiles from NAVGEM. The Fourier method is linear, accommodates realistic vertical variations in the background, and is similar to the Fourier method used previously by *Eckermann et al.* [2006] and *Alexander et al.* [2009] to model mountain waves generated by flow over island terrain. Their simulation extended to MLT altitudes. Figure 8a shows a sample Fourier-ray simulation of the wave-induced temperature perturbation field at 77 km altitude using the NAVGEM reanalysis profiles at 0600 UTC near the Auckland Islands, plotted for comparison with the AMTM zenith camera temperature fields in Figure 8b. The Fourier solution predicts large amplitudes, close to wave breaking, at these altitudes; see D. Broutman et al. (under review, 2016) for further details. The horizontal wavelength and basic orientation of the Fourier wavefield in Figure 8a are very similar to the AMTM observations in Figure 8b.

5. Conclusion

During the months of June and July 2014, the DEEPWAVE project took place in Christchurch, New Zealand. Taking advantage of the capabilities of the NSF GV aircraft, 26 research flights were performed during this

field campaign. One of the main goals of this project was the study of orographic wave deep propagation, from the troposphere to the MLT. On 14 July, favorable conditions were forecasted over the sub-Antarctic archipelago of Auckland Islands. Thus, research flight 23 was conducted to investigate the possible effects of orographic forcing on the middle and upper atmosphere. Oscillations in the vertical wind velocity, indicative of orographic waves being generated, were measured at flight altitude while the GV was approaching the lee side of the island. At the same time, a large-amplitude GW was observed in the MLT region, simultaneously by the IR imagers and the Na lidar operating on board the aircraft. This spectacular event remained at the same location during at least 4 h, before breaking and disappearing. Its huge momentum flux per unit mass (at least $320 \, m^2 \, s^{-2}$), estimated using direct measurements from the AMTM imager, the Na lidar, and the NAVGEM background profiles, implies a large effect of this localized wave event on the MLT region.

This is the first time that a minor orographic forcing due to moderate surface flow over small island terrain has been unambiguously related to GWs observed in the MLT, demonstrating its impact as high as 85 km of altitude. As it has been previously suggested [*Wu et al.*, 2006; *Alexander et al.*, 2009; *Vosper*, 2015], small islands may be indeed an important missing source of momentum flux deposition. Therefore, such waves need to be better accounted for in global circulation models to correctly parameterize wave drag in the middle and upper atmosphere.

References

Alexander, M. J., and A. W. Grimsdell (2013), Seasonal cycle of orographic gravity wave occurrence above small islands in the Southern Hemisphere: Implications for effects on general circulation, *J. Geophys. Res. Atmos.*, *118*, 11,589–11,599, doi:10.1002/2013JD020526.

Alexander, M. J., S. D. Eckermann, D. Broutman, and J. Ma (2009), Momentum flux estimates for South Georgia Island mountain waves in the stratosphere observed via satellite, *Geophys. Res. Lett.*, *36*, L12816, doi:10.1029/2009GL038587.

Aumann, H. H., et al. (2003), AIRS/AMSU/HSB on the Aqua mission: Design, science objectives, data products, and processing systems, *IEEE Trans. Geosci. Remote Sens.*, *41*, 253–264.

Bossert, K., et al. (2015), Momentum flux estimates accompanying multiscale gravity waves over Mount Cook, New Zealand, on 13 July 2014 during the DEEPWAVE campaign, *J. Geophys. Res. Atmos.*, *120*, 9323–9337, doi:10.1002/2015JD023197.

Bretherton, F. P. (1969), Momentum transport by gravity waves, *Q. J. R. Meteorol. Soc.*, *95*, 213–243.

Dewan, E. M., R. H. Picard, R. R. ONeil, H. A. Gardiner, J. Gibson, J. D. Mille, E. Richards, M. Kendra, and W. O. Gallery (1998), MSX satellite observations of thunderstorm-generated gravity waves in mid-wave infrared images of the upper stratosphere, *Geophys. Res. Lett.*, *25*, 939–942.

Dunkerton, T. J. (1987), Effect of nonlinear instability on gravity-wave momentum transport, *J. Atmos. Sci.*, *44*, 3188–3209.

Eckermann, S. D., and P. Preusse (1999), Global measurements of stratospheric mountain waves from space, *Science*, *286*, 1534–1537.

Eckermann, S. D., D. Broutman, J. Ma, and J. Lindema (2006), Fourier-ray modeling of short-wavelength trapped lee waves observed in infrared satellite imagery near Jan Mayen, *Mon. Weather Rev.*, *134*, 2830–2848.

Eckermann, S. D., K. W. Hoppel, L. Coy, J. P. McCormack, D. E. Siskind, K. Nielsen, A. Kochenash, M. H. Stevens, C. R. Englert, and M. Hervig (2009), High-altitude data assimilation system experiments for the northern summer mesosphere season of 2007, *J. Atmos. Sol. Terr. Phys.*, *71*, 531–551.

Eckermann, S. D., J. P. McCormack, J. Ma, T. F. Hogan, and K. A. Zawdie (2014), Stratospheric analysis and forecast errors using hybrid and sigma coordinates, *Mon. Weather Rev.*, *142*, 476–485.

Espy, P. J., R. E. Hibbins, G. R. Swenson, J. Tang, M. J. Taylor, D. M. Riggin, and D. C. Fritts (2006), Regional variations of mesospheric gravity-wave momentum flux over Antarctica, *Ann. Geophys.*, *24*, 81–88.

Fritts, D. C., and M. J. Alexander (2003), Gravity wave dynamics and effects in the middle atmosphere, *Rev. Geophys.*, *41*(1), 1003, doi:10.1029/2001RG000106.

Fritts, D. C., and G. D. Nastrom (1992), Sources of mesoscale variability of gravity waves. Part II. Frontal, convective, and jet stream excitation, *J. Atmos. Sci.*, *49*, 111–127.

Fritts, D. C., and R. A. Vincent (1987), Mesospheric momentum flux studies at Adelaide, Australia: Observations and a gravity wave/tidal interaction model, *J. Atmos. Sci.*, *44*, 605–619.

Fritts, D. C., S. A. Vadas, and Y. Yamada (2002), An estimate of strong local gravity wave body forcing based on OH airglow and meteor radar observations, *Geophys. Res. Lett.*, *29*(10), 1429, doi:10.1029/2001GL013753.

Fritts, D. C., P.-D. Pautet, K. Bossert, M. J. Taylor, B. P. Williams, H. Iimura, T. Yuan, N. J. Mitchell, and G. Stober (2014), Quantifying gravity wave momentum fluxes with Mesosphere Temperature Mappers and correlative instrumentation, *J. Geophys. Res. Atmos.*, *119*, 13,583–13,603, doi:10.1002/2014JD022150.

Fritts, D. C., et al. (2015), The Deep Propagating Gravity Wave Experiment (DEEPWAVE): An airborne and ground-based exploration of gravity wave propagation and effects from their sources throughout the lower and middle atmosphere, *Bull. Am. Meteorol. Soc.*, doi:10.1175/BAMS-D-14-00269.1.

Gardner, C. S., K. Gulati, Y. Zhao, and G. R. Swenson (1999), Measuring gravity wave momentum fluxes with airglow imagers, *J. Geophys. Res.*, *104*, 11,903–11,915.

Guest, F., M. Reeder, C. Marks, and D. Karoly (2000), Inertia-gravity waves observed in the lower stratosphere over Macquarie Island, *J. Atmos. Sci.*, *57*, 737–752.

Hendricks, E., J. M. Doyle, S. D. Eckermann, Q. Jiang, and P. A. Reinecke (2014), What is the source of the stratospheric gravity wave belt in austral winter?, *J. Atmos. Sci.*, *71*, 1583–1592, doi:10.1175/JAS-D-13-0332.1.

Hertzog, A., M. J. Alexander, and R. Plougonven (2012), On the intermittency of gravity wave momentum flux in the stratosphere, *J. Atmos. Sci.*, *69*(11), 3433–3448.

Hickey, M. P., and Y. Yu (2005), A full-wave investigation of the use of a "cancellation factor" in gravity wave-OH airglow interaction studies, *J. Geophys. Res.*, *110*, A01301, doi:10.1029/2003JA010372.

Hocke, K., and T. Tsuda (2001), Gravity waves and ionospheric irregularities over tropical convection zones observed by GPS/MET radio occultation, *Geophys. Res. Lett.*, *28*, 2815–2818.

Hogan, T. F., et al. (2014), The navy global environmental model, *Oceanography*, *27*(3), 116–125, doi:10.5670/oceanog.2014.73.

Hoppel, K. W., S. D. Eckermann, L. Coy, G. E. Nedoluha, D. R. Allen, S. D. Swadley, and N. L. Baker (2013), Evaluation of SSMIS upper atmosphere sounding channels for high-altitude data assimilation, *Mon. Weather Rev.*, *141*, 3314–3330.

Jewtoukoff, V., R. Plougonven, and A. Hertzog (2013), Gravity waves generated by deep tropical convection: Estimates from balloon observations and mesoscale simulations, *J. Geophys. Res. Atmos.*, *118*, 9690–9707, doi:10.1002/jgrd.50781.

Kim, Y.-J., S. D. Eckermann, and H.-Y. Chun (2003), An overview of the past, present, and future of gravity-wave drag parameterization for numerical climate and weather prediction models, *Atmos. Ocean*, *41*(1), 65–98.

Li, Z., A. Z. Liu, X. Lu, G. R. Swenson, and S. J. Franke (2011), Gravity wave characteristics from OH airglow imager over Maui, *J. Geophys. Res.*, *116*, D22115, doi:10.1029/2011JD015870.

Luo, Z., and D. C. Fritts (1993), Gravity-wave excitation by geostrophic adjustment of the jet stream. Part II: Three-dimensional forcing, *J. Atmos. Sci.*, *50*, 104–115.

Nappo, C. J. (2002), *Atmospheric Gravity Waves*, *Int. Geophys. Ser.*, vol. 85, Academic, San Diego, Calif.

Nastrom, G. D., and D. C. Fritts (1992), Sources of mesoscale variability of gravity waves. 1. Topographic excitation, *J. Atmos. Sci.*, *49*, 101–110.

Pautet, P.-D., M. J. Taylor, W. R. Pendleton Jr., Y. Zhao, T. Yuan, R. Esplin, and D. McLain (2014), An advanced mesospheric temperature mapper for high-latitude airglow studies, *Appl. Opt.*, *53*(26), 5934–5943.

Placke, M., P. Hoffmann, R. Latteck, and M. Rapp (2015), Gravity wave momentum fluxes from MF and meteor radar measurements in the polar MLT region, *J. Geophys. Res. Space Physics*, *120*, 736–750, doi:10.1002/2014JA020460.

Plougonven, R., H. Teitelbaum, and V. Zeitlin (2003), Inertia gravity wave generation by the tropospheric midlatitude jet as given by the Fronts and Atlantic Storm-Track Experiment radio soundings, *J. Geophys. Res.*, *108*(D21), 4686, doi:10.1029/2003JD003535.

Plougonven, R., A. Hertzog, and H. Teitelbaum (2008), Observations and simulations of a large-amplitude mountain wave breaking over the Antarctic Peninsula, *J. Geophys. Res.*, *113*, doi:10.1029/2007JD009739.

Reeder, M. J., and M. Griffiths (1996), Stratospheric inertia-gravity waves generated in a numerical model of frontogenesis. Part II: Wave sources, generation mechanisms and momentum fluxes, *Q. J. R. Meteorol. Soc.*, *122*, 1175–1195.

Sato, K., F. Hasegawa, and I. Hirota (1994), Short-period disturbances in the equatorial lower stratosphere, *J. Meteorol. Soc. Jpn.*, *72*, 859–872.

Sentman, D. D., E. M. Wescott, R. H. Picard, J. R. Winick, H. C. Stenbaek-Nielsen, E. M. Dewan, D. M. Moudry, F. T. São Sabbas, M. J. Heavner, and J. Morrill (2003), Simultaneous observations of mesospheric gravity waves and sprites generated by a mid-western thunderstorm, *J. Atmos. Sol. Terr. Phys.*, *65*, 537–550.

Smith, S. M., J. Baumgardner, and M. Mendillo (2009), Evidence of mesospheric gravity-waves generated by orographic forcing in the troposphere, *Geophys. Res. Lett.*, *36*, L08807, doi:10.1029/2008GL036936.

Swenson, G. R., R. Haque, W. Yang, and C. S. Gardner (1999), Momentum and energy fluxes of monochromatic gravity waves observed by an OH imager at Starfire Optical Range, New Mexico, *J. Geophys. Res.*, *104*, 6067–6080.

Tang, J., A. Z. Liu, and G. R. Swenson (2002), High frequency gravity waves observed in OH airglow at Starfire Optical Range, NM: Seasonal variations in momentum flux, *Geophys. Res. Lett.*, *29*(20), 1966, doi:10.1029/2002GL015794.

Taylor, M. J., and M. A. Hapgood (1988), Identification of a thunderstorm as a source of short period gravity waves in the upper atmospheric nightglow emissions, *Planet. Space Sci.*, *36*(10), 975–985.

Tsuda, T., M. Nishida, C. Rocken, and R. H. Ware (2000), A global morphology of gravity wave activity in the stratosphere revealed by the GPS occultation data (GPS/MET), *J. Geophys. Res.*, *105*, 7257–7273.

Vadas, S. L., and D. C. Fritts (2002), The importance of spatial variability in the generation of secondary gravity waves from local body forces, *Geophys. Res. Lett.*, *29*(20), 1984, doi:10.1029/2002GL015574.

Vadas, S. L., and M. J. Nicolls (2009), Temporal evolution of neutral, thermospheric winds and plasma response using PFISR measurements of gravity waves, *J. Atmos. Sol. Terr. Phys.*, *71*, 744–770.

Vadas, S. L., M. J. Taylor, P.-D. Pautet, P. A. Stamus, D. C. Fritts, H.-L. Liu, F. T. São Sabbas, V. T. Rampinelli, P. P. Batista, and H. Takahashi (2009), Convection: The likely source of the medium-scale gravity waves observed in the OH airglow layer near Brasilia, Brazil, during the SpreadFEx campaign, *Ann. Geophys.*, *27*, 231–259.

von Savigny, C., I. C. McDade, K.-U. Eichmann, and J. P. Burrows (2012), On the dependence of the OH* Meinel emission altitude on vibrational level: SCIAMACHY observations and model simulations, *Atmos. Chem. Phys. Discuss.*, *12*, 5817–5849.

Vosper, S. B. (2015), Mountain waves and wakes generated by South Georgia: Implications for drag parametrization, *Q. J. R. Meteorol. Soc.*, doi:10.1002/qj.2566.

Wu, D. L., and J. W. Waters (1996), Satellite observations of atmospheric variances: A possible indication of gravity waves, *Geophys. Res. Lett.*, *23*, 3631–3634.

Wu, D. L., P. Preusse, S. D. Eckermann, J. H. Jiang, M. de la Torre Juarez, L. Coy, and D. Y. Wang (2006), Remote sounding of atmospheric gravity waves with satellite limb and nadir techniques, *Adv. Space Res.*, *37*, 2269–2277.

Yamada, Y., H. Fukunishi, T. Nakamura, and T. Tsuda (2001), Breakdown of small-scale quasi-stationary gravity wave and transition to turbulence observed in OH airglow, *Geophys. Res. Lett.*, *28*, 2153–2156.

Yeh, K. C., and C. H. Liu (1981), The instability of atmospheric gravity waves through wave-wave interactions, *J. Geophys. Res.*, *86*, 9722–9728.

Yiğit, E., and A. S. Medvedev (2010), Internal gravity waves in the thermosphere during low and high solar activity: Simulation study, *J. Geophys. Res.*, *115*, A00G02, doi:10.1029/2009JA015106.

Yue, J., S. Vadas, C.-Y. She, T. Nakamura, S. Reising, H.-L. Liu, P. Stamus, D. Krueger, W. Lyons, and T. Li (2009), Concentric gravity waves in the mesosphere generated by deep convective plumes in the lower atmosphere near Fort Collins, *J. Geophys. Res.*, *114*, D06104, doi:10.1029/2008JD011244.